Life Cycle of Numerically Simulated Shallow Cumulus Clouds. Part II: Mixing Dynamics

MING ZHAO* AND PHILIP H. AUSTIN

Atmospheric Science Programme, Department of Earth and Ocean Sciences, University of British Columbia, Vancouver, British Columbia, Canada

(Manuscript received 2 June 2003, in final form 1 September 2004)

ABSTRACT

This paper is the second in a two-part series in which life cycles of six numerically simulated shallow cumulus clouds are systematically examined. The six clouds, selected from a single realization of a large-eddy simulation, grow as a series of pulses/thermals detached from the subcloud layer. All six clouds exhibit a coherent vortical circulation and a low buoyancy, low velocity trailing wake. The ascending cloud top (ACT), which contains this vortical circulation, is associated with a dynamic perturbation pressure field with high pressure located at the ascending frontal cap and low pressure below and on the downshear side of the maximum updrafts. Examination of the thermodynamic and kinematic structure, together with passive tracer experiments, suggests that this vortical circulation is primarily responsible for mixing between cloud and environment. As the cloud ACTs rise through the sheared environment, the low pressure, vortical circulation, and mixing are all strongly enhanced on the downshear side and weakened on the upshear side. Collapse of the ACT also occurs on the downshear side, with subsequent thermals ascending on the upshear side of their predecessors. The coherent core structure is maintained throughout the ACT ascent; mixing begins to gradually dilute the ACT core only in the upper half of the cloud's depth. The characteristic kinematic and dynamic structure of these simulated ACTs, together with their mixing behavior, corresponds closely to that of shedding thermals. These shallow simulated clouds, however, reach a maximum height of only about four ACT diameters so that ACT mixing differs from predictions of self-similar laboratory thermals.

1. Introduction

This paper continues the investigation of the life cycle of numerically simulated shallow cumulus clouds begun in Zhao and Austin (2005, hereafter Part I). In Part I we describe the large-eddy simulation (LES) case setup, the isolation of individual cloud life cycle data from the simulated cloud field, and the use of a tracer to identify the cloud-mixed convective region. We examine in detail the mass and thermodynamic transport associated with the life cycle of individual clouds with special emphasis on the unsaturated part of cumulus convection, the impact of buoyancy on the cloud vertical convective transport, and the role of cloud size in the cloud ensemble transport. Part II continues this investigation using the same set of six clouds. Our focus in Part II is on understanding the details of the simulated cumulus mixing dynamics, particularly the mixing associated with the active ascending cloud elements. Our objective is to produce a qualitative and quantitative description of the simulated cloud mixing life cycle that can be compared against the conceptual models that form the basis of parameterizations of shallow cumulus cloud mixing and transport (e.g., Arakawa and Schubert 1974; Emanuel 1991; Zhao 2003).

Detailed aircraft measurement of the structure of ordinary cumulus clouds date back to the work of Stommel (1947), Malkus (1954), Warner (1955), and Warner and Squires (1958). These observations have established that the properties of such clouds cannot be explained solely by the adiabatic ascent of air from cloud base. The observations indicated that the horizontally averaged liquid water content and buoyancy of cumulus clouds are far smaller than their respective adiabatic values. It is natural to assume that most of the departure from adiabatic is due to mixing through the cloud sides. The observations showed, however, that there is little systematic variation in cloud properties across a cloud and that dry holes occur frequently in the bases of clouds, in contrast to laboratory plumes (e.g., Warner

* Current affiliation: NOAA/Geophysical Fluid Dynamics Laboratory, Princeton, New Jersey.

Corresponding author address: Dr. Ming Zhao, NOAA/Geophysical Fluid Dynamics Laboratory, Princeton University, Forrestal Campus, Box 308, U.S. Route 1, Princeton, NJ 08542.
E-mail: ming.zhao@noaa.gov

1955). Later observations showed that undilute subcloud air (USCA) occurs in all levels within cumulus clouds (e.g., Heymsfield et al. 1978; Jensen et al. 1985; Austin et al. 1985). These measurements raised doubts about the validity of treating clouds as entraining plumes. For example, Warner (1970) pointed out that it was impossible for such models to simultaneously reproduce realistic values of liquid water content and cloud-top height (the cloud-top liquid water paradox); if the entrainment rate is adjusted to predict the observed height, then the predicted liquid water content is much too high.

On the other hand, Squires (1958) proposed that the turbulent mixing of dry environmental air near the tops of clouds can result in substantial negative buoyancy; this may cause strong penetrative downdrafts. Emanuel (1981) showed that the penetrative downdrafts may be potentially as strong or stronger than convective updrafts. Squires argued that vertical penetrative downdrafts rather than horizontal mixing was the principal mechanism responsible for cumulus cloud dilution. Squire's hypothesis received some support from the observations of Paluch (1979), who used two conserved variables to deduce the environmental origin of air sampled by glider inside Colorado cumuli. The interiors of these nonprecipitating cumuli were shown to be extremely inhomogeneous, with some samples corresponding to nearly undilute ascent cloud-base air and others composed of various mixtures of subcloud air with environmental air from near cloud top. These results were corroborated by a number of other studies (e.g., Boatman and Auer 1983; Jensen et al. 1985). However, it is difficult to imagine how cloud updrafts could be constrained to entrain only upon reaching their ultimate tops.

Using the analysis technique of Paluch (1979), Blyth et al. (1988) examined more than 80 Montana cumuli and found that the source of entrained air was close to, or slightly above, the observation height of the aircraft at many different levels in the clouds. This result suggests that the entrainment process in growing clouds is modified cloud-top entrainment, where cloud top means the ascending cloud top (ACT) of the growing cloud. These and other considerations motivated Blyth et al. to propose a conceptual cloud model based on a shedding thermal. In this model, entrainment occurs near the ACT, and mixed parcels subsequently descend around the edge of the advancing thermal core into a trailing wake region driven by a toroidal circulation. While supporting the idea of ascending cloud-top entrainment, Jonas (1990) presented a different picture in which the environmental air from near cloud top is transported in a thin, subsiding layer to lower levels and is then entrained laterally into the cloud. The cloud tracer experiments of Stith (1992) give some support to this latter picture. Although these in situ studies have provided insight into cumulus mixing dynamics, there is still no general agreement on the detailed mechanism by which air enters and is mixed into a cumulus cloud (Blyth 1993).

Laboratory studies of buoyant plumes and thermals, together with similarity assumptions, have provided another tool to understand cumulus mixing. Conceptual cumulus models based on bubbles/thermals were proposed by Scorer and Ludlam (1953) and Scorer and Ronne (1956). These and other laboratory experiments (e.g., Scorer 1957; Woodward 1959) showed that thermals mix environmental fluid into their tops as well as through their wakes during their ascent. Furthermore, Scorer and Ronne found that parts of thermals were sometimes shed into the wake in a stratified ambient fluid. This led them to propose a shedding thermal model of the sort later adopted by Blyth et al. (1988). More recently, Johari (1992) found that entrainment occurs as ambient fluid moves in thin sheets around the perimeter of the thermals and enters through the rear of the thermal. This is in contrast to the classical picture of mixing taking place along the advancing front of the thermal (Scorer 1958) and (as mentioned above) is supported by the in situ observations of Jonas (1990) and Stith (1992). Johari also noted the presence of unmixed ambient fluid deep inside the thermal, captured not by small-scale motions along the thermal's leading edge but by the larger-scale motion set up by the advancing vortical circulation. He concluded that it is the large-scale vortical circulation associated with the global motion of the thermal that dominates entrainment and mixing.

Laboratory experiments have illustrated the detailed flow structure of individual thermals in an idealized environment. Cumulus clouds, however, differ from laboratory thermals in several respects. Specifically, they are characterized by 1) phase change, which can produce either positive or negative buoyancy through condensation or mixing and evaporation; 2) environmental wind and wind shear; 3) subcloud buoyancy fluctuations that are continuously generated from a turbulent boundary layer; 4) ambient vertically varying stratification; and 5) Reynolds numbers that are far larger than those that can be produced in current tank experiments.

High-resolution numerical simulation is a third tool that has been increasingly used to study both individual cumulus dynamics and cumulus ensemble statistics. Numerous cloud simulations attempt to model the evolution and structure of one or a few convective clouds. Typically, these models assume an atmosphere that possesses a given quantity of convective available potential energy, which is released over a limited period by the clouds. Klaassen and Clark (1985) used a specified surface heat flux and a 2D model with interactive grid nesting to examine in detail the entrainment mechanism of a small cumulus cloud. They found that small-scale horizontal density gradients were responsible for the onset of cloud–environment interface instabilities, while evaporative cooling played only a mi-

nor role in mixing. Grabowski and Clark (1993) extended these simulations to 3D and obtained results similar to those of Klaassen and Clark, indicating that dynamical effects rather than evaporation are more significant in cumulus entrainment.

Carpenter et al. (1998a) pointed out difficulties with a simple specification of the surface heat flux, arguing that fully turbulent motion in the boundary layer is required to produce realistic cloud entrainment. They first arbitrarily generate turbulent motion on all resolvable scales and then reduced the heat flux to more realistic values. Carpenter et al. used this initialization and a nested mesh with an inner 50-m resolution to study the entrainment and detrainment in New Mexican cumulus congestus. The authors conducted parcel trajectory and conserved variable analyses of the modeled clouds and found that cumulus entrainment and detrainment is primarily associated with the ascending cloud top and its induced toroidal circulation. Their results lend some support to the shedding thermal model previously described in Blyth et al. (1988).

In contrast to these individual cloud simulations, an LES is continually forced by specified large-scale conditions, and many convective clouds are simulated over a sufficient period so that they collectively come into equilibrium with the forcing. Unless multiple equilibria are possible, an LES can be expected to reach a statistical steady state that is independent of initial conditions (Emanuel 1994). Therefore, an LES provides an alternative approach to generate cumulus clouds with fully developed boundary layer turbulence in a more realistic large-scale environment, albeit with some sacrifice of model resolution. We can select individual clouds from an equilibrium convective field and apply passive numerical tracers to systematically diagnose the isolated cloud mixing behavior. In this paper we make a first attempt to examine in detail the mixing dynamics of convective elements generated in these LES fields, using the six clouds described in Part I. This analysis complements the cloud in situ observations, laboratory tank experiments, and previous numerical simulations that have motivated a variety of conceptual models of cumulus mixing.

In Part I, section 2, we describe the LES, the Barbados Oceanic and Meteorological Experiment (BOMEX) initial conditions and forcings, and the procedures used to distinguish convective clouds from the environment. To review briefly: the simulation was performed with the Colorado State University System for Atmospheric Modeling (Khairoutdinov and Randall 2003) on a model domain of 6.4 km $\times$ 6.4 km $\times$ 3.2 km. We isolated six clouds (labeled A–F) with cloud-top heights ranging from 1 to 2 km and used a numerical tracer to track the evolution of both the saturated cloud and the unsaturated cloud-mixed region.

In section 2a of this paper, we present the pulsating behavior of the simulated cumulus growth. The cloud growth rate and thermal turnover time are quantified in section 2b. In section 2c, we present the cloud kinematic structure, cloud-top vortical circulation, and an elevated tracer experiment for cumulus entrainment. In section 2d, we link the cloud-top vortical circulation to the baroclinic torque and present the perturbation pressure field. The dilution rate and the mixture distribution in the ascending cloud top are quantified in section 2e. The continued mixing between low-buoyancy, low-vertical-velocity cloud mixtures and the environment is briefly described in section 2f. In section 3 we discuss a picture of cumulus mixing that is consistent with the simulation results.

2. Results

a. Pulsating cloud growth

Animations of clouds A–F (Zhao and Austin 2004) show that an individual cloud consists of one or more coherent updraft pulses/thermals that grow and decay over 10 to 15 min periods. Small clouds (A, B, C) have a single ascending pulse that dissipates without reaching the inversion. Large clouds (D, E, F) consist of a series of pulses, each of which detaches from a subcloud layer thermal, strengthens in the middle of the cloud layer, and collapses after reaching a maximum height within or below the inversion. The first pulse of these large clouds is the strongest, reaching its maximum height within the inversion, while the subsequent pulses are weaker and attain maximum heights lower than their predecessors. There is also a tendency for an elongated pulse to break into two elements, with the lower element strengthening when the upper one collapses after reaching its maximum height. In this case, the lower pulse always develops on the upshear side while the upper pulse collapses into the downshear side. The pulsating character of cloud growth is most distinct beginning at about 400 m above the cloud base ($\sim$1 km above the surface). All of the pulse elements tend to become dynamically detached[1] from their subcloud layer parent thermals some distance above cloud base.

Figure 1 shows an example of this pulsating ascent as viewed at a fixed cloud level for cloud E. When the updraft first arrives at the 1237.5-m level at 500 s, it brings a large proportion of relatively undilute subcloud air, producing the largest anomalies of liquid water potential temperature θ_l, total water q_t, virtual potential temperature θ_v, and vertical velocity w for both the cloud mean value (dashed line) and the most undilute cloud grid cell (i.e., the grid cell extreme value: solid line). Between 500 and 800 s these values quickly

[1] Here, by dynamically detached, we mean the pulse elements will not be significantly influenced by the cloud air below, since these elements ascend faster and tend to distance themselves from the cloud material below.

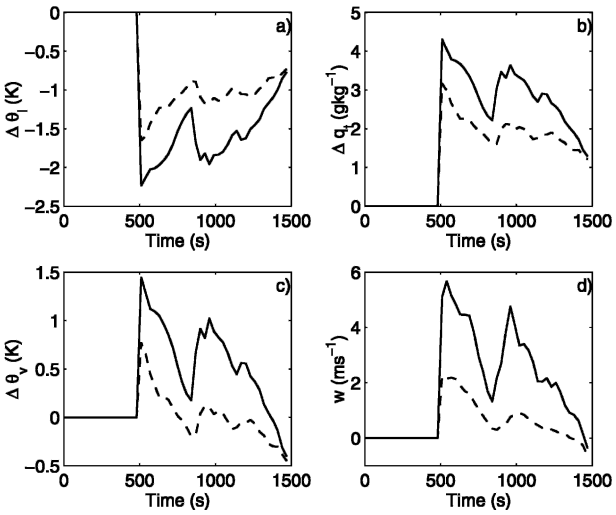

FIG. 1. An example of the pulsating character of cloud E. (a) Dashed line: time evolution of $\Delta\theta_l$, the θ_l difference between liquid water cloud horizontal mean and environment at height 1237.5 m. Solid line: the θ_l difference between the most undilute cloud grid cell and environment. (b) As in (a) but for q_t. (c) As in (a) but for θ_v. (d) As in (a) but for vertical velocity w.

decrease (θ_l increases) as more dilute cloud mixtures with low vertical velocities are left in the trailing wake of the advancing top. Further mixing with environmental air tends to continually dilute these cloud mixtures until the next ascending thermal penetrates this level and brings a new anomaly at approximately 1000 s. Cloud E dissipates following the second pulse.

Figure 2 shows this pulsating structure at all cloud levels as time–height contours of θ_l, q_t, θ_v, and w of the most undilute cloud parcel. The two growth pulses, which are spaced approximately 500 s apart, are present at all cloud levels above 1 km. The second pulse is weaker and moves upward less rapidly than the initial thermal. The structure of the second pulse is harder to discern in the mean fields (not shown) because it ascends into the remnants of the previous thermal. Due to this difficulty in separating a pulse from the remnants of previous thermals, we limit the following analysis to the first thermal for each cloud. This initial thermal is the simulated counterpart to the ascending turret of a developing cloud, and will be referred to below as the ascending cloud top (ACT). The sharp contrast between an ACT and its environment makes it easy to isolate, particularly with the use of a subcloud layer tracer as described in section 2c of Part I.

Animation of the entire simulated cloud field shows that pulsating growth is a characteristic feature of all simulated clouds. This is consistent with numerous observational studies describing the growth of cumulus clouds either as individual bubbles or as a collection of multiple bubbles (e.g., Ludlam and Scorer 1953; Malkus and Scorer 1955; Saunders 1961; Blyth et al. 1988; Blyth and Latham 1993; Barnes et al. 1996; French et al. 1999). Pulsating cloud growth is also reported in other high-resolution numerical simulations of isolated cumulus clouds (e.g., Carpenter et al. 1998a).

These single cloud simulations, however, typically discard the early phase of the convective clouds in which the ACT is most easily isolated. This is necessary due to the unrealistic boundary layer turbulence and ambient environment caused by the model's initial lack of motion on all resolvable scales (Carpenter et al. 1998a). In contrast, for the LES-ensemble cloud simulation presented here, individual clouds develop from a fully turbulent boundary layer that is in equilibrium with the large-scale environment. With the isolation technique described in Part I, we can obtain uncontaminated 5-dimensional simulation data for the ACT of each selected cloud. These pseudoclouds provide an excellent opportunity to investigate the kinematics and dynamics of the ACT and its mixing behavior. In the following sections we begin with a description of the bulk properties of the ACT and then examine in detail the kinematic structure and dynamics of the ACT for clouds A–F.

b. Growth rate and thermal turnover time scale

The cloud-top height $z_T(t)$ (the maximum height that contains liquid water at time t) was shown in Part I (Fig. 5a) to increase at an approximately exponential rate during the growth phase of individual clouds. To quantify the difference between clouds A–F, Fig. 3a reproduces Fig. 5a of Part I in semilogarithmic coordinates. There is a near-linear dependence of $\log(z_T)$ on time t for all clouds, motivating the definition of the ACT growth rate α as

$$\alpha = \frac{d(\log z_T)}{dt}, \tag{1}$$

where α is determined by a linear fit to $d(\log z_T)/dt$ from Fig. 3a during the growth phase. A vertical length scale of an ACT may be chosen as the maximum height $z_{T,\max}$ achieved by the ACT. Figure 3b shows the variation of growth rate α versus $z_{T,\max}$. This growth rate tends to vary near-linearly with $z_{T,\max}$, with the ACTs of larger clouds having higher growth rates. The solid line in Fig. 3b is a linear least squares fit of α to $z_{T,\max}$ for the six clouds. Since the growth rate α is nearly constant during an individual ACT ascent (Fig. 3a) the thermal turnover time t_* can be computed by integrating (1)

$$t_* = \int_{z_{T,0}}^{z_{T,\max}} \frac{1}{\alpha}\, d\log(z_T) = \frac{1}{\alpha}\log\left(\frac{z_{T,\max}}{z_{T,0}}\right), \tag{2}$$

where $z_{T,0} = z_B$ represents the cloud-top height when it first emerges from the subcloud layer. Figure 3c shows the ACT thermal turnover time for the six clouds; with

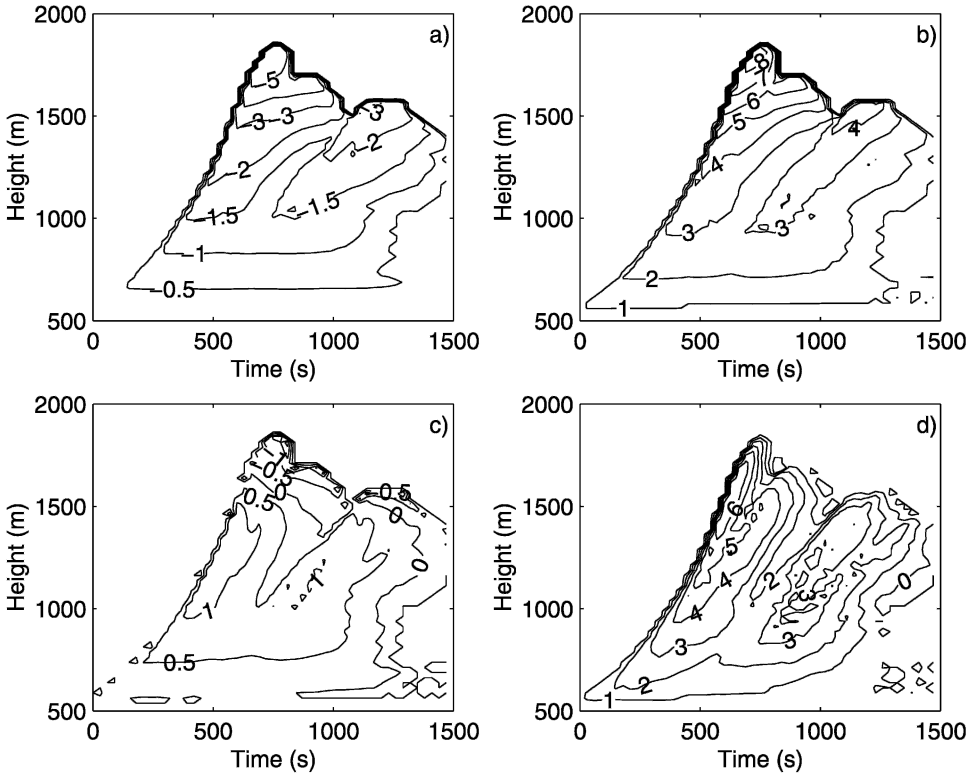

FIG. 2. Time–height variation of the differences ($\Delta\theta_l$, Δq_t, $\Delta\theta_v$, Δw) for the most undilute grid cell for cloud E: (a) θ_l (K) difference between the most undilute grid cell and environment. (b) As in (a) but for q_t (g kg^{-1}). (c) As in (a) but for θ_v (K). (d) As in (a) but for vertical velocity w (m s^{-1}).

the exception of cloud C, all clouds have approximately the same thermal turnover time of 600 s (solid line).

Our 600-s t_* represents the average time required for air in a turret (ACT) to travel from cloud base to maximum cloud top. Neggers et al. (2002) used instantaneous snapshots of an LES shallow cumulus cloud field to determine a similar time scale for a given idealized parcel ascending through a cloud's depth. They averaged the vertical velocity along the three-dimensional path of the strongest updraft in a particular cloud. They then used the ratio of the cloud depth to this averaged maximum vertical velocity to estimate τ_c, the time required for the air in the strongest updraft to rise from cloud base to cloud top. Using a cloud population with a range of thicknesses, they found $\tau_c = 300$ s to be approximately independent of cloud depth (as do we: when we follow the maximum updraft for our six clouds, we also find an approximate time constant of $\tau_c = 350$ s that is roughly independent of cloud depth). The larger value of t_* determined from Fig. 3 indicates that air contained within the coherent structure of the ACT does not simply rise along the instantaneous maximum vertical velocity in the cloud field. Rather it tends to be vertically constrained and circulates within the ACT, rising on average with about half the speed of the major updrafts. In the next section we show this coherent circulation more explicitly.

c. Kinematic structure of the ACT

Individual ascending thermals have a spatial scale smaller than the cloud envelope. Observational studies of the kinematic structure of these ascending thermals is difficult, due primarily to their highly transient nature (Blyth et al. 1988). They are, however, the building blocks of individual clouds and hence the cloud ensemble and, therefore, play a fundamental role in cumulus convective transport and cloud environment mixing. Below we examine in detail the kinematic structure of the first ascending thermal, that is, the ACT of the simulated clouds. We use cloud E as an example to illustrate characteristic features present in all six selected clouds.

Figure 4 shows vertical cross sections (x–z plane) of the resolved wind vectors from cloud E at 7.5, 8.5, 9.5, and 10.5 min after emergence from the subcloud layer. The ambient mean wind $u_0 = -7.5$ m s^{-1} and the vertical velocity of the ascending cloud–environment interface, $w_T(t)$ (where the subscript T indicates the current cloud-top height) have been subtracted from the corresponding velocity field. The $w_T(t)$ at each time step is found using the growth rate $\alpha_E = 0.0017$ s^{-1} from Fig. 3b and the current cloud-top height z_T via (1); that is, $w_T(t) = dz_T(t)/dt = \alpha_E z_T(t)$. A distinct vortical circulation exists within the top part of the growing cloud

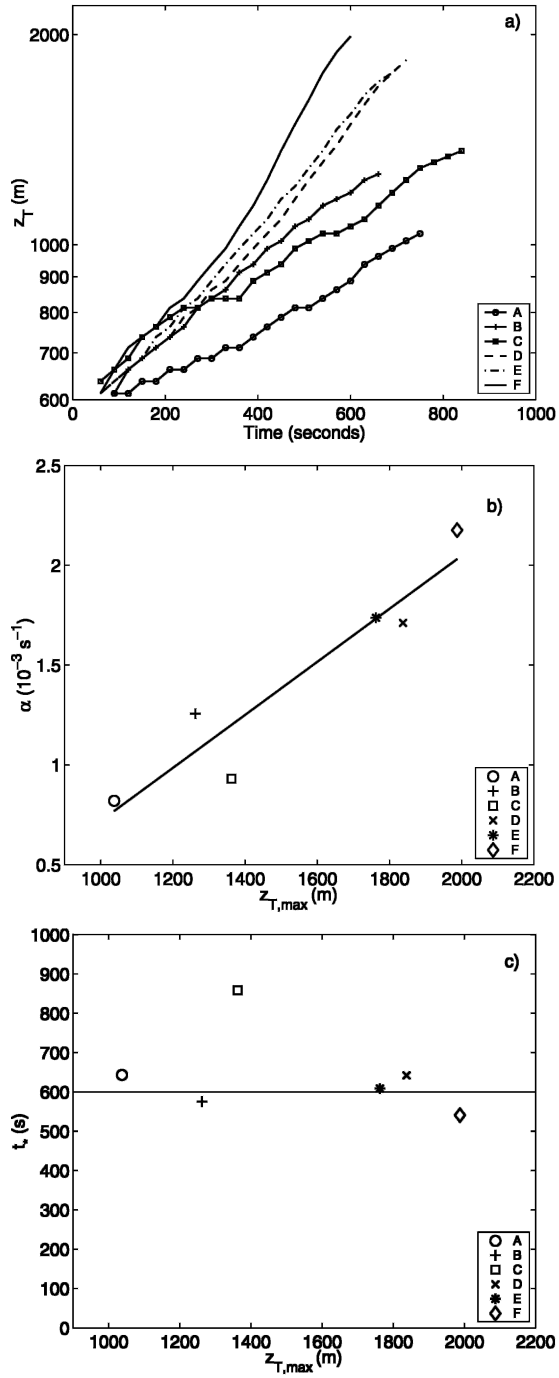

FIG. 3. (a) Time evolution of the ascending cloud-top height z_T for clouds A–F. (b) The growth rate α vs maximum cloud-top height $z_{T,\max}$ for each cloud. (c) The thermal turnover time t_* vs maximum cloud-top height $z_{T,\max}$ for each cloud. Solid line: average t_* neglecting cloud C.

[approximately 14 model levels (350 m) below z_T], which is seen in 3-dimensional visualizations to consist of ascent along the central (not strictly axisymmetric) vertical axis and descent around the periphery.

Below this coherent internal circulation, the cloud-top relative vertical velocity (denoted as CT-relative below) is generally near zero or negative (i.e., Figs. 4a–d at 800, 900, 1000, and 1200 m). Air parcels located below these levels generally cannot approach the moving cloud top given this resolved flow. Motivated by this distinct kinematic structure, we define the ACT as the upper part of the growing cloud; it encompasses the coherent vortical circulation. We will refer to the region below the ACT, which is more dilute and has low vertical velocity, as the trailing wake of the advancing ACT. The cloud–environment mixtures in the trailing wake will also be called passive cloud mixtures below to distinguish them from the active cloud mixtures within the ACT. In addition, we will refer to the shallow, frontal cap of the ACT, which extends about 4 to 6 model levels below the cloud–environment interface and has strong horizontal divergence, as the ascending frontal cap (AFC; see box, Fig. 4a). Note that the AFC represents the top edge of the ascending liquid cloud rather than the updrafts. Therefore, it has a mean vertical velocity close to the ascending speed of the cloud–environment interface.

As Fig. 4 shows, there is a strong updraft core in the center of the ACT with maximum vertical velocity approximately twice that of the AFC mean vertical velocity (or equivalently, w_T). The core updraft velocity is gradually reduced to near zero (CT- relative) within the AFC, which results in strong horizontal divergence. Near the edge of the ACT there is a distinct overturning circulation with downward CT-relative vertical velocity roughly equal to that of the central updrafts. The overall internal circulation is weak when the ACT just emerges from subcloud layer (Fig. 4a), is gradually strengthened in the middle of the cloud layer (Figs. 4b,c,d), and tends to be rapidly weakened after penetration of the inversion layer.

Before we discuss how the vortical circulation influences the cloud entrainment and mixing, we show in Fig. 5 the vortical circulation in y–z cross sections cut along the $x = 550$ m lines of Fig. 4. Clearly, the coherent ACT vortical circulation is three-dimensional although it is not axisymmetric; the downshear side circulation is more complete while the upshear side circulation tends to be weakened (note that the ambient wind shear in the north–south direction diminishes above 1 km). We will discuss this asymmetrical ACT vortical circulation and the ambient shear later in this section and in section 2d.

To examine how the vortical circulation influences ACT–environment mixing, we release a tracer η with a uniform mixing ratio of $\eta = 1$ g kg^{-1} in an elevated layer between 1100 and 1200 m prior to the ACT penetration of this layer (Fig. 4a). Figure 4b shows that, when the ACT reaches the tracer layer, it displaces ambient fluid upward while ambient η is incorporated into a thin layer by direct contact with the ACT surface. The entrained air does not, however, continually erode

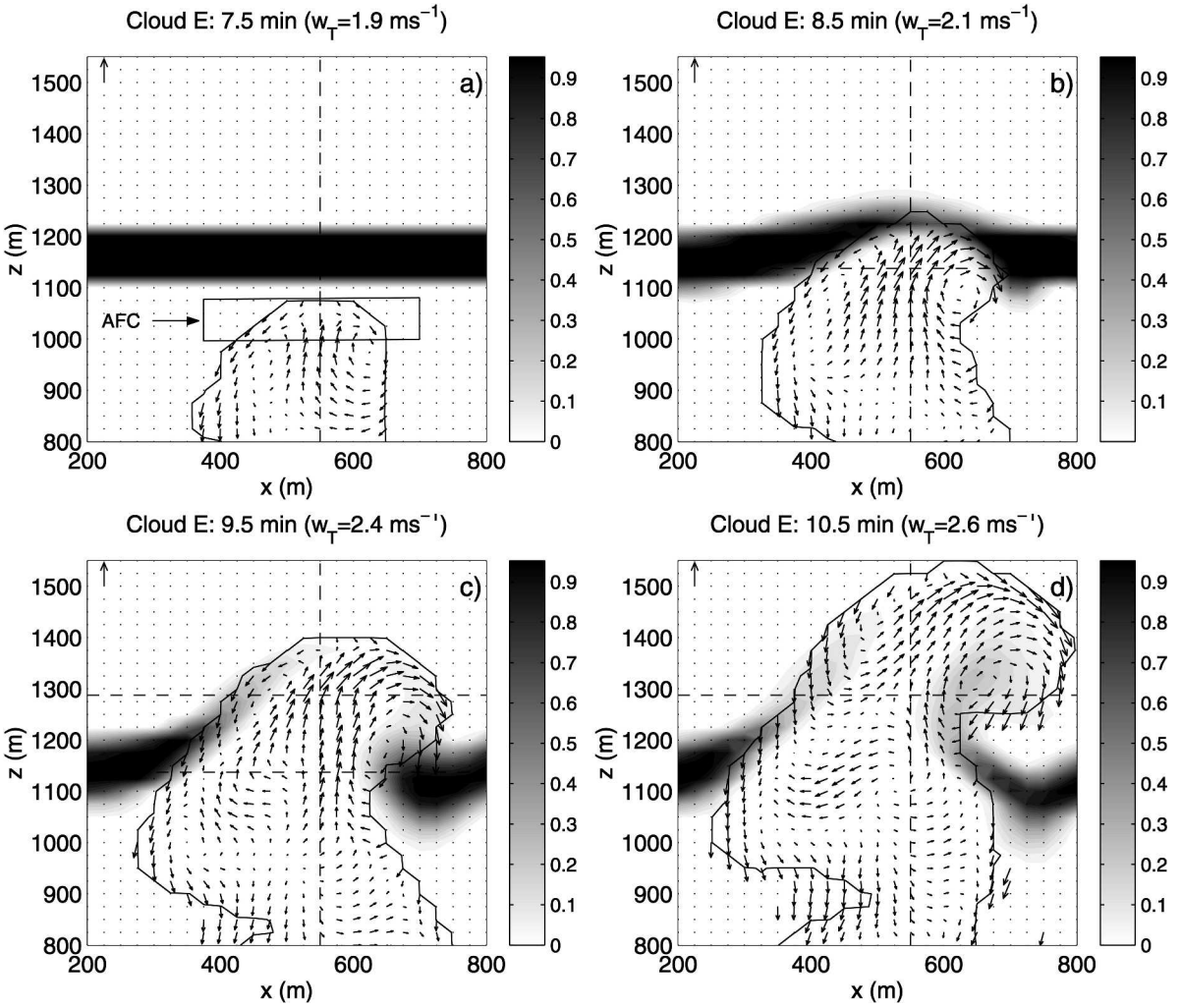

FIG. 4. Vertical cross section (x–z slices cut following the y = 650 m lines in Fig. 5) of the internal flow pattern within the ACT of cloud E at 7.5, 8.5, 9.5, and 10.5 min after emerging from the subcloud layer. Solid line: $q_c > 0.01$ g kg^{-1} contour. Arrows: u–w wind vectors for the convective mixed region defined in section 2c of Part I (wind vectors outside this region are masked). The ambient mean wind $u_0 = -7.5$ m s^{-1} has been subtracted from horizontal velocity u while the cloud-top vertical velocity w_T has been subtracted from the vertical velocity w for each panel. The vertical shear of the horizontal mean wind is from left (west) to right (east) as shown in Fig. 1c of Part I. The arrows at the top left corner of each panel show the vertical velocity scale (3.8 m s^{-1}). Shading: the mixing ratio of a tracer η, which is initially uniform (η = 1 g kg^{-1}) between 1100 and 1200 m at the 7.5-min time step. Dashed lines of constant x indicate the x coordinates of the y–z slices of Fig. 5. Dashed lines of constant z indicate the z coordinates of the x–y slices of Fig. 6.

into the center of the ACT but is, instead, advected downward along the edge to the rear of the ACT (e.g., Figs. 4b and 4c, at 1100 to 1200 m) leaving a nearly η-free AFC after the penetration (Figs. 4c and 4d). Environmental air entrained through the ACT top, after being circulated to the ACT rear, is further mixed into the ACT center through the vortical circulation (Fig. 4d, downshear side between 1200 and 1400 m). The strong AFC divergence prevents any deep erosion of the ACT core from the ACT top, while the circulation along the ACT edge tends to quickly remove the more dilute cloud mixtures from the AFC, leaving the AFC as the most active and buoyant region throughout the ascent. In general, these simulation results support the schematic shedding thermal model proposed by Blyth and coauthors (e.g., Blyth et al. 1988; Blyth 1993).

Environmental air is also directly engulfed into the ACT from the ACT rear through an organized vortical circulation on a large scale (comparable to ACT size). Figure 6 shows x–y cross sections of the horizontal velocity field at two different vertical levels and three different times. Figures 6a and 6b show the horizontal cross sections at a level 1137.5 m. Wind vectors are overlaid with the shaded contour of liquid water mixing ratio q_c. At 8.5 min this 1137.5-m level is 75 m below the current cloud-top height [z_T (8.5 min) = 1212.5 m]. The flow field reflects the AFC mass divergence; no clear resolvable-scale entraining eddies appear. The mixing

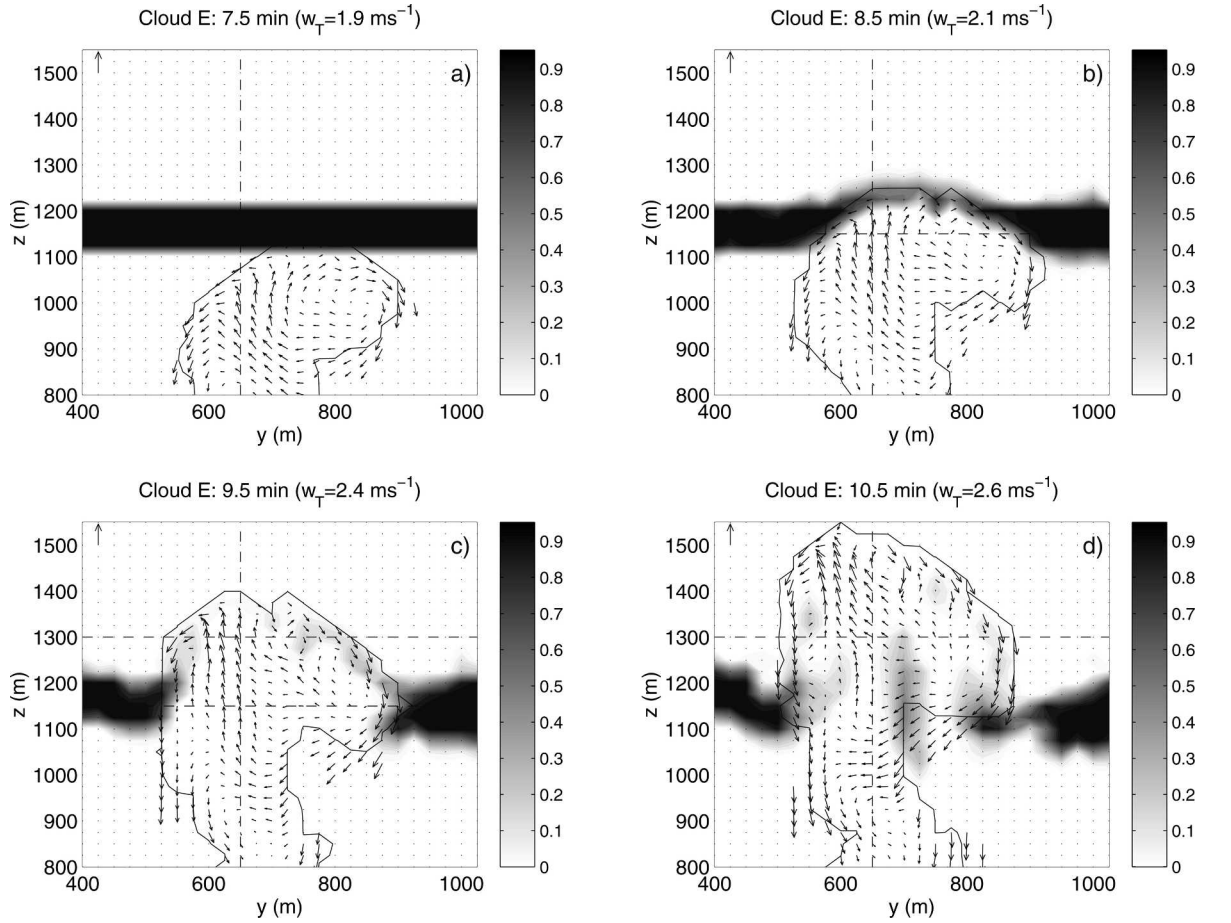

FIG. 5. As in Fig. 4 except these are y–z cross sections cut following the x = 550 m lines in Fig. 4. Arrows: v–w wind vectors for the convective mixed region defined in section 2c of Part I. The ambient mean wind v_0 is from right (north) to left (south) with the shear direction point to north; v_0 is small and is not subtracted from v. The arrows at the top left corner of each panel show the scale for vertical velocity 4.1 m s^{-1}. Dashed lines of constant y indicate the y coordinate of the x–z slices of Fig. 4. Dashed lines of constant z indicate the z coordinates of the x–y slices of Fig. 6.

along the edge of cloud and environment is primarily through the parameterized subgrid-scale eddy diffusion. At 9.5 min this same level now samples the ACT rear [z_T (9.5 min) = 1362.5 m]; Fig. 6b shows the clear indication of resolvable-scale entraining eddies.

The circulation along these horizontal slices indicates that the vorticity vector is not strictly along the horizontal plane (Figs. 4 and 5), as predicted for an idealized vortex ring or a spherical vortex, but also has a vertical component (Fig. 6). These entraining eddies have scales comparable to the ACT size itself and they directly engulf the environmental air and move it deep into the ACT center. Figures 6c,d show horizontal slices through another vertical level (1287.5 m) at 9.5 and 10.5 min. We observe a pattern similar to that shown in Figs. 6a,b. Notice that the engulfment of environmental air from the ACT rear is located on the downshear side [east (right) of the cloud] in this sheared environment. Overall, there is a net convergence at the ACT rear, in contrast to the net divergence at the ACT top (or AFC).

In contrast to the ACT upper-interface mixing, which is primarily driven by subgrid-scale eddies, the ACT rear entrainment is primarily through resolvable large-scale entraining eddies. In comparison, these large-scale eddies associated with the vortical circulation must dominate the entrainment and mixing of the simulated clouds throughout their ascent. Furthermore, the mixed parcels first entrained from either the ACT top or sides are carried by the vortical circulation to the ACT rear where some of the mixtures are further wrapped into the vortex center, while others may stay behind depending on their vertical velocity and buoyancy. Therefore, the coherent vortical circulation strongly modulates the ACT's entrainment and mixing of environmental air.

The effect of ambient wind shear on the ACT's vortical circulation and mixing can also be seen in Figs. 4 and 5. The vertical shear of the horizontal mean wind is from west (left) to east (right) in Fig. 4 and from south (left) to north (right) in Fig. 5. Comparing the four

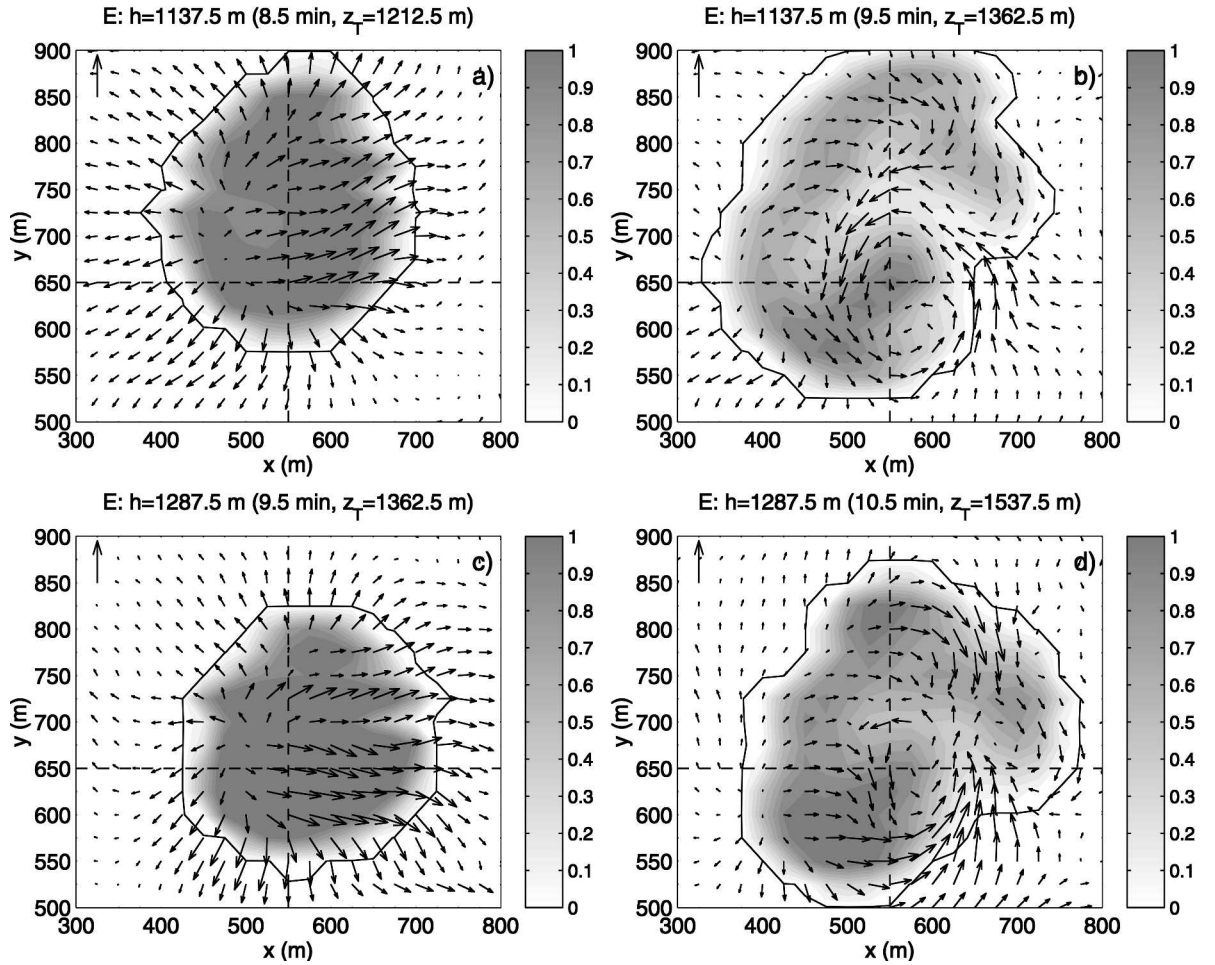

FIG. 6. Horizontal cross section cut following the horizontal lines shown in Figs. 4 and 5. Solid line: $q_c > 0.01$ g kg^{-1} contour. Arrows: u–v wind vectors. The ambient mean wind $u_0 = -7.5$ m s^{-1} has been subtracted from the horizontal velocity u. The arrows at the top left corner of each panel show the vertical velocity scale 2.3 m s^{-1}. Shading: the liquid water mixing ratio q_c (g kg^{-1}). Dashed lines of constant y indicate the y coordinate of the x–z slices of Fig. 4. Dashed lines of constant x indicate the x coordinate of the y–z slices of Fig. 5.

panels in Fig. 4 and also the four panels in Fig. 5 shows that, when the ACT rises through the sheared environment, the vortical circulation is continuously tilted toward the downshear side with the downshear-side circulation enhanced while the upshear side is weakened. For this reason, the overall ACT mixing and subsequent mixing-induced downdrafts are enhanced at the downshear side of the cloud [note the unsaturated downdrafts (arrows outside the $q_c > 0.01$ g kg^{-1} contour) on the downshear side of the cloud in Figs. 4c,d and Figs. 5a–d]. The ACT eventually collapses to the downshear side after penetrating the inversion, while newly developed thermals ascend through the upshear side of the cloud (not shown).

This ambient shear effect can be understood by examining the ambient vorticity field produced by the vertical shear of the horizontal mean wind. For example, in Fig. 4 the ambient vorticity vector points northward (into the page) and, hence, has the same sign as the downshear side vorticity but with sign opposite that of the upshear side vorticity. The vorticity at both sides is horizontal and parallel to the ambient vorticity. Thus, the ambient vorticity enhances the downshear-side circulation while weakening the upshear-side circulation. Note, however, that the ACT vortical circulation is three-dimensional. When the horizontal vorticity is parallel to the ambient shear vector, the effect of the ambient wind shear is to tilt the horizontal vorticity toward the vertical, which can be seen from the tilting/twisting term of the vorticity equation (e.g., Holton 1992). Therefore, the ambient shear is ultimately responsible for the generation of the horizontal entraining eddies shown in Figs. 6b,d. In section 2d, we will further explore some dynamics of the vortical circulation.

Figure 7 shows the time–height variation of the horizontal mass divergence of the liquid water cloud region (left panels) and convective mixed region (right panels) for the large clouds D, E, and F. For all three clouds,

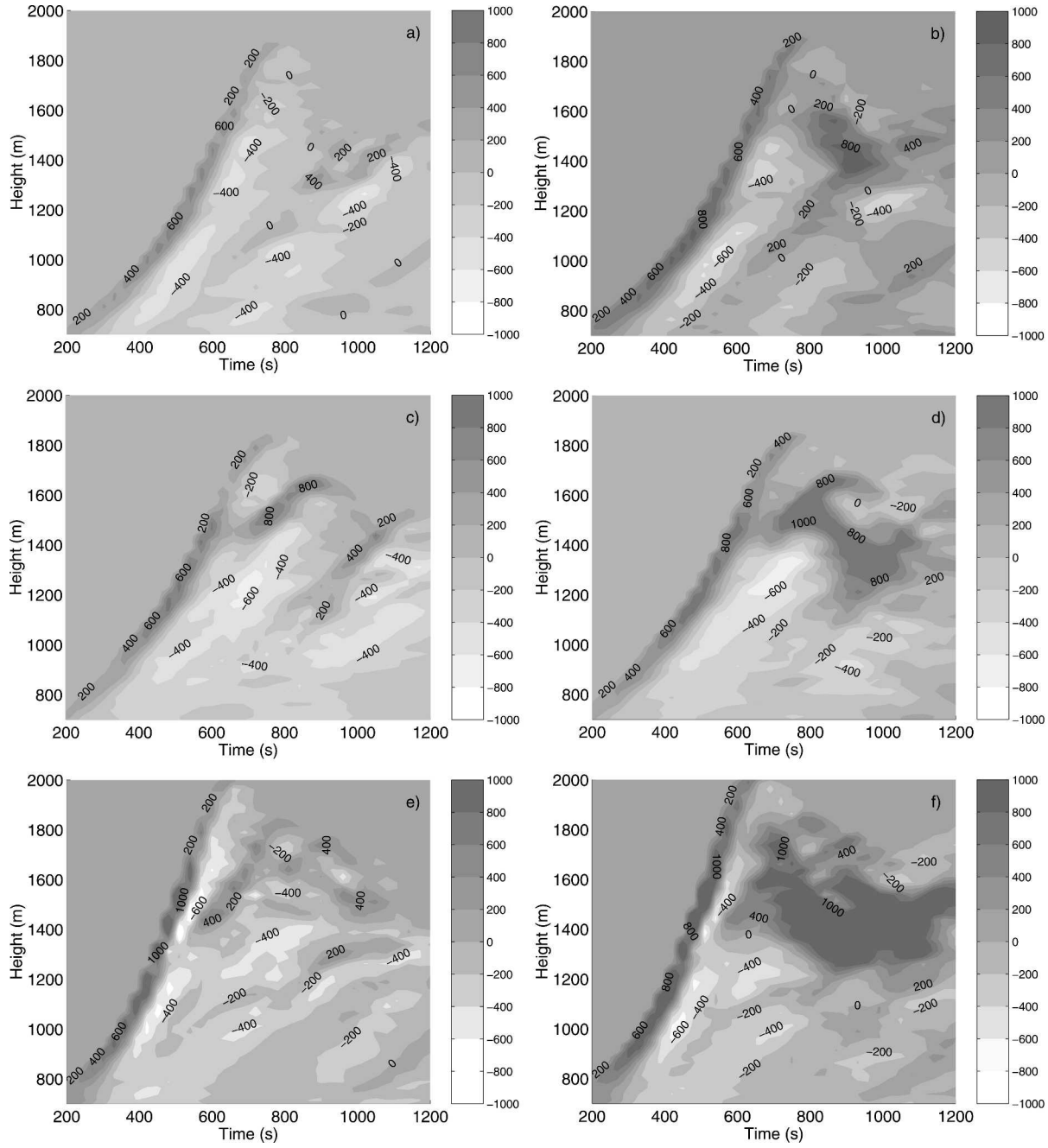

FIG. 7. Time–height variation of the air–mass horizontal divergence {i.e., contours of $D_{t,k}$ (kg m^{-1} s^{-1}) = $\int_A - [\partial(\rho w)/\partial z]dA$ for time step t, vertical level k} integrated over different cloud areas A: (a) A calculated for the liquid water cloud region of cloud D. (b) As in (a) but for convective mixed region. (c) As in (a) but for cloud E. (d) As in (b) but for cloud E. (e) As in (a) but for cloud F. (f) As in (b) but for cloud F.

the divergence zone associated with the shallow AFC is evident throughout the ACT ascent between roughly 200 and 600 s; it overlays a relatively thick convergence zone that ascends with the cloud top. After penetrating the inversion at ~600 s, the strength of the convergence and divergence pattern is weakened. When the ACTs reach their maximum height at ~700 to 800 s they collapse and accelerate downward; this, together with the subsequent arrival of ascending thermals, produces a strong divergence zone near the inversion base. When comparing the left and right panels of Fig. 7 we see large areas of strong divergence (dark-shaded region at approximately 1300 to 1600 m after 800 s) on the right panels that are absent from the left panels. This indi-

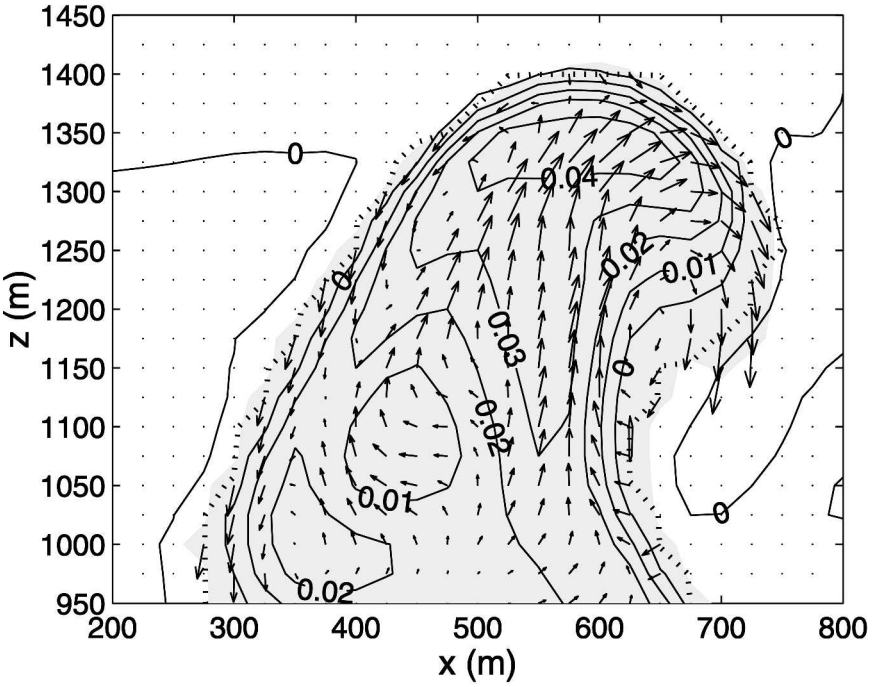

FIG. 8. The cross section of Fig. 4c but with contours of the buoyancy B (m s^{-2}). The convective mixed region is shaded. Thick dotted line: $q_c > 0.01$ g kg^{-1} contour. Arrows as in Fig. 4c.

cates that the persistent divergence zone occurs primarily in the unsaturated convective mixed region following the collapse of the ACTs. As we will show in section 2e, the strong divergence is associated with the detrainment of cloud–environment mixtures at the layer where the cloud buoyancy decreases with height. This preferential detrainment is consistent with both the buoyancy-sorting detrainment hypothesis of Raymond and Blyth (1986) and the numerical and analytical results of Bretherton and Smolarkiewicz (1989) and Taylor and Baker (1991), which indicate that cloud detrainment occurs at levels with decreasing cloud buoyancy.

While the simulated ACTs present a complex three-dimensional structure of the vortical circulation, the general pattern in which ascent is along the central vertical axis and descent is around the periphery is consistent with the laboratory results of ascending thermals, in situ observations of cumulus clouds, and the conceptual shedding thermal model proposed by Blyth et al. (1988) (Scorer 1957; Johari 1992; Stith 1992; Carpenter et al. 1998b). The impact of ambient wind shear on the simulated clouds is furthermore consistent with observational evidence showing that downdrafts and mixing occur preferentially on the downshear side of a cloud, while updrafts tend to persist on a cloud's upshear side (e.g., Warner 1977).

d. Dynamical structure of the ACT

To obtain more insight into the internal circulation and mixing behavior of the ACT, we need to further examine its dynamics. In this section, we first examine the buoyancy field in the simulated ACT and explain the simulated vortical circulation using the concept of baroclinic torque. We thenfurther examine the perturbation pressure field and partition it into dynamic and buoyancy components following Wilhelmson and Ogura (1972).

1) BUOYANCY DISTRIBUTION AND BAROCLINIC TORQUE

Figure 8 shows the buoyancy contours of the cross section of Fig. 4c. We see a mushroom-shaped buoyant core (e.g., 0.03 m s^{-2} contour) that consists of the AFC centered at 1300 m and a trailing stem located within the ACT between 1100 and 1250 m. There is a strong horizontal buoyancy gradient, particularly at the downshear side (note the negatively buoyant area at the downshear side of cloud edge). During the ascent of the ACT, more buoyant parcels at the ACT center tend to move rapidly upward while the less buoyant parcels at the ACT edge tend to move more slowly. This horizontal buoyancy difference provides a net torque that acts to rotate the cloud parcels clockwise on the right-hand side and anticlockwise on the left-hand side of the buoyancy maximum in Fig. 8.

The baroclinic torque and its role in generating the horizontal vorticity can be seen from a two-dimensional (x–z plane) vorticity equation derived under the Boussinesq approximation, which is valid for this shallow

convection case (although the actual LES equations are anelastic):

$$\frac{d\omega}{dt} = \frac{\partial \omega}{\partial t} + \left(u \frac{\partial \omega}{\partial x} + w \frac{\partial \omega}{\partial z} \right) = \omega \left(\frac{\partial u}{\partial x} + \frac{\partial w}{\partial z} \right) - \frac{\partial B}{\partial x}, \tag{3}$$

where u and w are the wind components along the x and z directions respectively, B is buoyancy, and $\omega = (\partial u/\partial z - \partial w/\partial x)$ is the vorticity component perpendicular to the x–z plane, with positive vorticity pointing into the page (Fig. 8). The vorticity production terms on the rhs of (3) are due respectivelyto the divergence and the horizontal buoyancy gradient. If the system initially contains no vorticity ($\omega = 0$), the only vorticity production term comes from the horizontal buoyancy-gradient term.

From Fig. 8, we see that the buoyancy-gradient term should produce positive ω on the right-hand side of the buoyancy maximum and negative ω on the left-hand side of the buoyancy maximum, consistent with the simulation results. This buoyancy-gradient term can be formally related to the solenoidal term in the general vorticity equation (e.g., Holton 1992). The solenoidal term involves the density difference along a constant pressure surface and is generally called the baroclinic torque (e.g., Klaassen and Clark 1985). Here, this density difference is primarily due to the cloud condensational heating. The strong horizontal buoyancy gradient in the simulated clouds indicates that the baroclinic torque is primarily responsible for the generation of the vortical circulation of the simulated ACTs. While the baroclinic torque may be the primary source for the initial production of the vorticity for the simulated ACTs, this initially horizontal vorticity, as discussed in section 2c, must also be redistributed into vertical vorticity in the sheared environment (when the horizontal vorticity component is parallel to the shear vector). This will result in large ACT-scale horizontal eddies which might further break into smaller-scale eddies. This is a probable explanation for the complex three-dimensional structure of the entraining eddies shown in Figs. 4–6.

2) PERTURBATION PRESSURE

Figures 9a–c show the same vertical cross section as in Fig. 8 but with contours of perturbation pressure p, the vertical component of the perturbation pressure gradient force (PPGF) ($\text{PPGF}_v = (-\rho^{-1}\partial p/\partial z)$, and the sum of PPGF_v and B. The subgrid-scale momentum flux term is, in general, a small term compared with either PPGF_v or B and will be neglected below. Figure 9a shows a high pressure region centered on the AFC at 1380 m with a low pressure region below and on the downshear (right) side of the vertical velocity maximum at 1200 m. Notice the tendency for the perturbation pressure contours to parallel the wind vectors around the vortical circulation.

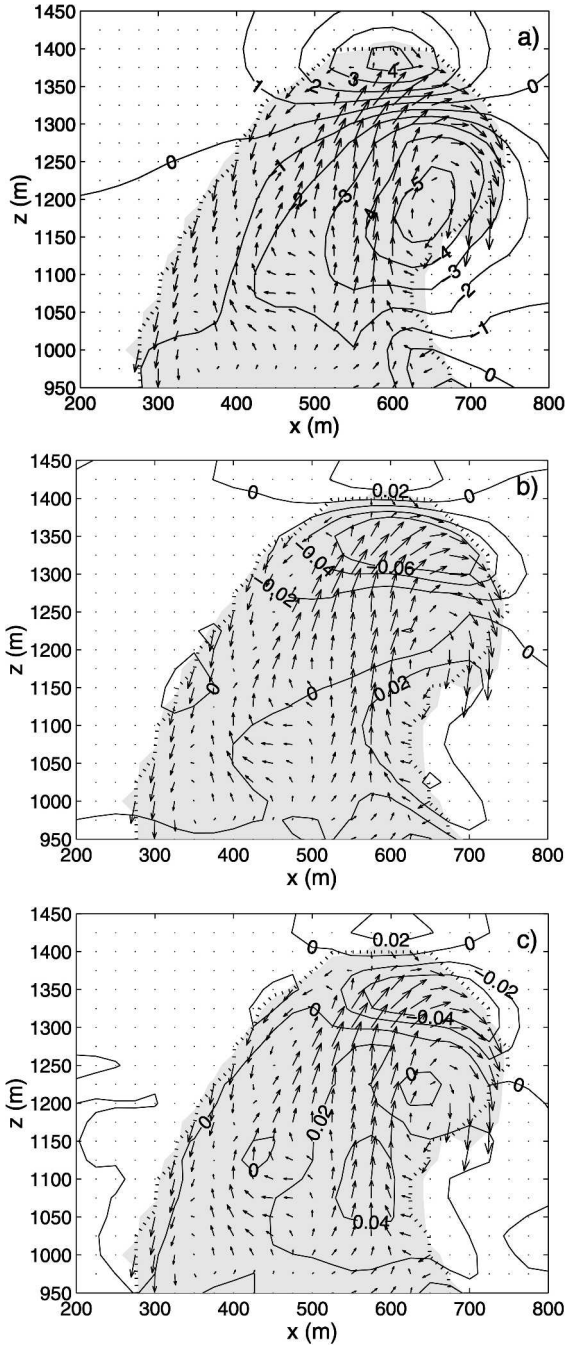

FIG. 9. (a) As in Fig. 8, but with contour of perturbation pressure field p (Pa). Arrows as in Fig. 4c. (b) As in (a) but with contours of PPGF_v (m s^{-2}). (c) As in (a) but with contours of $\text{PPGF}_v + B$ (m s^{-2}).

The ACT, accelerating into the quiescent environment, produces a perturbation pressure field that tends to slow down its ascent (see Fig. 9b). Figure 9c shows that near the shallow AFC region (1300 to 1400 m) the PPGF_v is larger in magnitude than the buoyancy force and produces a net downward force, indicating that the

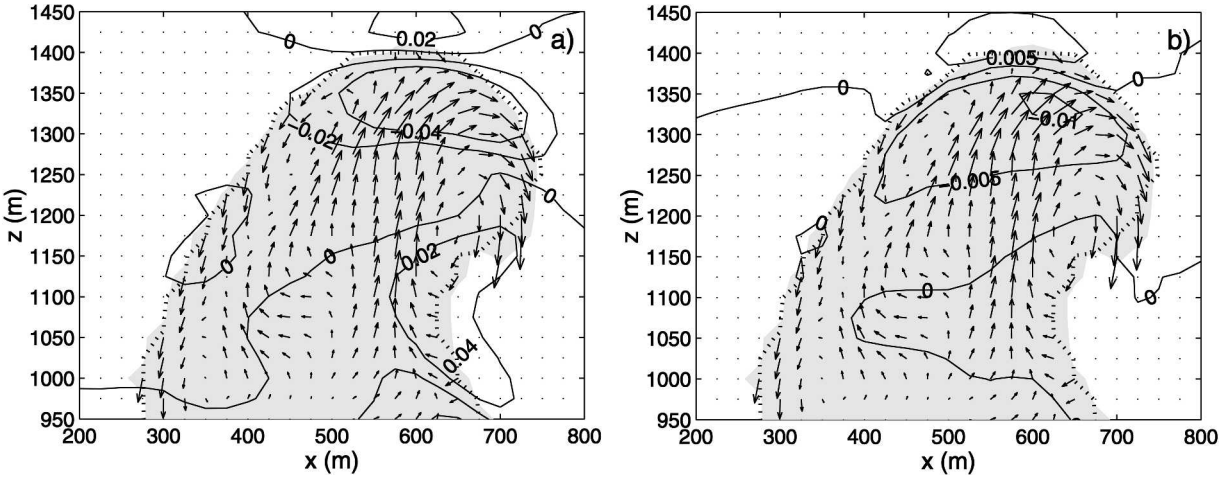

FIG. 10. (a) As in Fig. 9b but with $PPGF_v$ replaced by $PPGF_d$ (m s^{-2}). (b) As in (a) but with $PPGF_d$ replaced by $PPGF_b$ (m s^{-2}).

vertical momentum flux into the AFC must be positive in order to maintain its ascent. This net downward force experienced by individual parcels works effectively to cap the fast moving parcels and is associated with their overturning motion within the ACT. Due to this net downward force, the most buoyant parcels decelerate and spread outward as they approach the AFC. Mixing with surrounding air along the leading edge of the ACT tends to dilute cloud parcels exposed to the environment, while evaporation rapidly reduces their buoyancy. When these parcels circulate downward along the ACT edge to the ACT rear (i.e., between 1050 and 1200 m in Fig. 9c) the combined effect of the downward circulation, dilution, and evaporation produces large values of the CT-relative downward vertical velocity.

By continually shedding these cloud–environment mixtures, the AFC region remains the most buoyant part of the ACT throughout its ascent. The CT-relative downward transport of mixed air and the enhanced entrainment due to the vortical circulation at the rear of the thermal tends to push the more buoyant core into a comparatively narrow shaft below the AFC. This tends to intensify the horizontal buoyancy gradient and produces stronger vortical circulation. This is consistent with the fact that the vortical circulation is strengthened throughout its ascent in the cloud layer (below the inversion).

Below we further explore the perturbation pressure by partitioning it into dynamical and buoyancy components following Wilhelmson and Ogura (1972). The diagnostic equation for the perturbation pressure under the anelastic approximation may be written as (Wilhelmson and Ogura 1972):

$$\frac{\partial^2 p}{\partial x_i^2} = \underbrace{-\frac{\partial}{\partial x_i}\left(\frac{\partial \rho u_i u_j}{\partial x_j} + \frac{\partial \tau_{ij}}{\partial x_j}\right)}_{\text{I}} + \underbrace{\frac{\partial \rho B}{\partial x_i}\delta_{i3}}_{\text{II}}, \tag{4}$$

where p is the nonhydrostatic perturbation pressure, $\rho = \rho(z)$ is the base state mean density that varies only with altitude. Here, u_i ($i = 1, 2, 3$) are the resolved wind components along the x, y, and z directions respectively; τ_{ij} is the subgrid-scale momentum ρu_i flux in the j direction. The equation is written in summation notation and repeated indices are summed. Following Wilhelmson and Ogura (1972), the first two terms on the rhs are labeled the dynamic contribution (I) and the third term is labeled the buoyancy contribution (II) to the p Laplacian. Since (4) is linear in p, the total perturbation pressure p can be decomposed into the dynamic perturbation pressure p_d and the buoyancy perturbation pressure p_b. These two terms can be found by solving

$$\frac{\partial^2 p_d}{\partial x_i^2} = \text{I} \tag{5a}$$

$$\frac{\partial^2 p_b}{\partial x_i^2} = \text{II}. \tag{5b}$$

Figures 10a,b show the partitioned dynamic PPGF [$PPGF_d = (-\rho^{-1}\partial p_d/\partial z]$ and buoyancy PPGF [$PPGF_b = (-\rho^{-1})\partial p_b/\partial z]$ which sum to the total $PPGF_v$ shown in Fig. 9b. Both PPGFs are negative and act to decelerate the air parcels within the AFC. However $PPGF_d$ is nearly one order of magnitude larger than $PPGF_b$ within the AFC. Thus, p_d is expected to largely determine the distribution of the total perturbation pressure p within the ACT. A contour plot of p_d (not shown) indicates that it does indeed have a very similar pattern to that of Fig. 9a.

In section 2c we have described the impact of the ambient shear on the ACT's vortical circulation and ACT entrainment. The impact of this ambient wind shear on the dynamic perturbation pressure field can also be seen in Fig. 9a; it enhances the low pressure region on the downshear side of the ACT while dimin-

ishing or weakening the low pressure region on the upshear side.

e. Dilution of the ACT

In section 2c we defined the ACT as the upper part of the growing cloud containing the vortical circulation. To quantify the dilution rate of the ACT we sample it by choosing all the saturated grid cells located in the 14 model levels below z_T ($\Delta h = 350$ m below the current z_T) for large clouds and the 7 model levels below z_T ($\Delta h = 175$ m below the current z_T) for small clouds. These vertical limits generally include the cloud-top vortical circulation for each of the six selected clouds. The ACT mean properties are computed by averaging all selected grid cells. We also define the most undilute core within the ACT (called the ACT core below) as the average of the $2 \times 2 \times 2$ grid cells that have the largest $\Delta q_t = q_{t,c} - \langle q_t \rangle$, where $q_{t,c}$ denotes the total water of a cloudy grid cell and $\langle q_t \rangle$ is the horizontal model domain averaged q_t. Similarly, the most dilute cloudy parcels within the ACT are defined as the average of the $2 \times 2 \times 2$ grid cells that have the smallest Δq_t. These two statistics are used as a measure of ACT inhomogeneity. Since an ACT ascends with time, the time histories of an ACT's mean properties may be directly converted to vertical profiles of those properties based on the time-dependent height. Thus, the vertical profiles of the ACT properties presented below show the time evolution of the ACT in a Lagrangian frame of reference.

Figure 11 shows the vertical profiles (time histories) of buoyancy (given as the virtual potential temperature difference $\Delta\theta_v = \theta_{v,c} - \langle\theta_v\rangle$) for the ACT mean (solid), the ACT core (dashed), and the most dilute air within ACT (dot–dash). The vertical height at a given time is taken as the average geometric center of each category of grid cells. The vertical profile of cloud-mean buoyancy, which is calculated by averaging over the entire life cycle for all liquid water containing grid cells at each level, is also plotted (dotted) for comparison. First, we see that the interior of the ACT is nonhomogeneous for all six clouds; the ACT core remains nearly undilute during much of its ascent (see also Fig. 12), thus producing large positive buoyancy values. In contrast, the most dilute cloudy grid cells are negatively buoyant throughout the ACT ascent for all clouds. Although not as buoyant as the ACT core, the ACT mean is systematically more buoyant than the cloud mean (dotted). The buoyancy excess of the ACT mean in comparison with the cloud mean is significant, considering that the cloud mean is only marginally buoyant. For large clouds, the cloud-mean buoyancy becomes negative at roughly 150 m below the inversion base (Figs. 11d–f).

In the literature, the cloud-top height and cloud vertical velocity are usually determined by the cloud-mean buoyancy assuming a steady state. When integrating $w\partial w/\partial z = B(z)$, with $B(z)$ determined from the cloud-mean buoyancy, we find that the resulting velocity profile (not shown) always underestimates the cloud-top height. This is expected since cloud growth is associated with the ACT properties rather than the cloud-mean properties, which may be significantly biased to low values by the passive cloud mixtures detrained from the active ascending ACT. This result is consistent with the liquid water/cloud-top paradox first noted by Warner (1970). Figures 11d–f show, in contrast, that for the large clouds the ACT mean is significantly more buoyant and maintains its positive buoyancy up to the base of the inversion, while the most buoyant ACT cores maintain their positive buoyancy up to the middle of the inversion. These clouds ascend as long as their ACT core is positively buoyant; therefore the dilution rate of the ACT core is particularly relevant to the determination of the cloud-top height. Also shown in Figs. 11d–f is the fact that large clouds overshoot their ACT core NBL by roughly 200 m.

Figures 12a,b show the vertical profiles (time histories) of θ_l and q_t for the ACT core for each cloud. For comparison, we also plot on Figs. 12a,b the vertical profiles of θ_l and q_t calculated based on an entraining plume model. Figures 12a,b show the dilution rate for the large clouds (D, E, F) is less than that for the smaller clouds (A, B, C) for both conserved variables. For the largest cloud F, the ACT core is diluted at a rate approximately equal to an entrainment rate 0.0003 m^{-1} (dotted line); this is the entrainment rate used in the cumulus parameterization scheme of Tiedtke (1989). Although, as Siebesma and Cuijpers (1995) point out, this entrainment rate is one order of magnitude smaller than the dilution rate for the cloud-mean properties; it better predicts the dilution rate of the ACT core and thus the cloud-top height. However, as Figs. 12a,b show, the shapes of the vertical profiles of θ_l and q_t for the ACT core still differ qualitatively from those predicted by an entraining plume, because the ACT cores experience no dilution until they reach the upper half of their $z_{T,\max}$. Figures 12c,d further show that, with the exception of cloud A, when the profiles are normalized by the individual cloud depth they collapse into a single profile, showing that the ACT cores stay essentially unmixed in the lower half of their depth and are gradually diluted in the upper half of their depth.

While individual clouds may achieve very different cloud-top heights, they have nearly the same cloud-root thermodynamic properties. This can be seen from Figs. 12a,b, where the cloud-base θ_l and q_t for all clouds are nearly the same [although large clouds tend to be slightly moister (0.1–0.3 g kg^{-1} in Fig. 12b) than small clouds]. Given this, the dilution rates (and, therefore, cloud-top heights) are most probably caused by differences in ACT size. Indeed, as Fig. 13 shows, the ACTs of large clouds (D, E, F) are nearly twice as big as those of the small clouds (A, B, C) when measured in terms of the ACT volume-equivalent spherical radius. However, it is likely that this size dependency will be diminished when an ACT exceeds a threshold size large

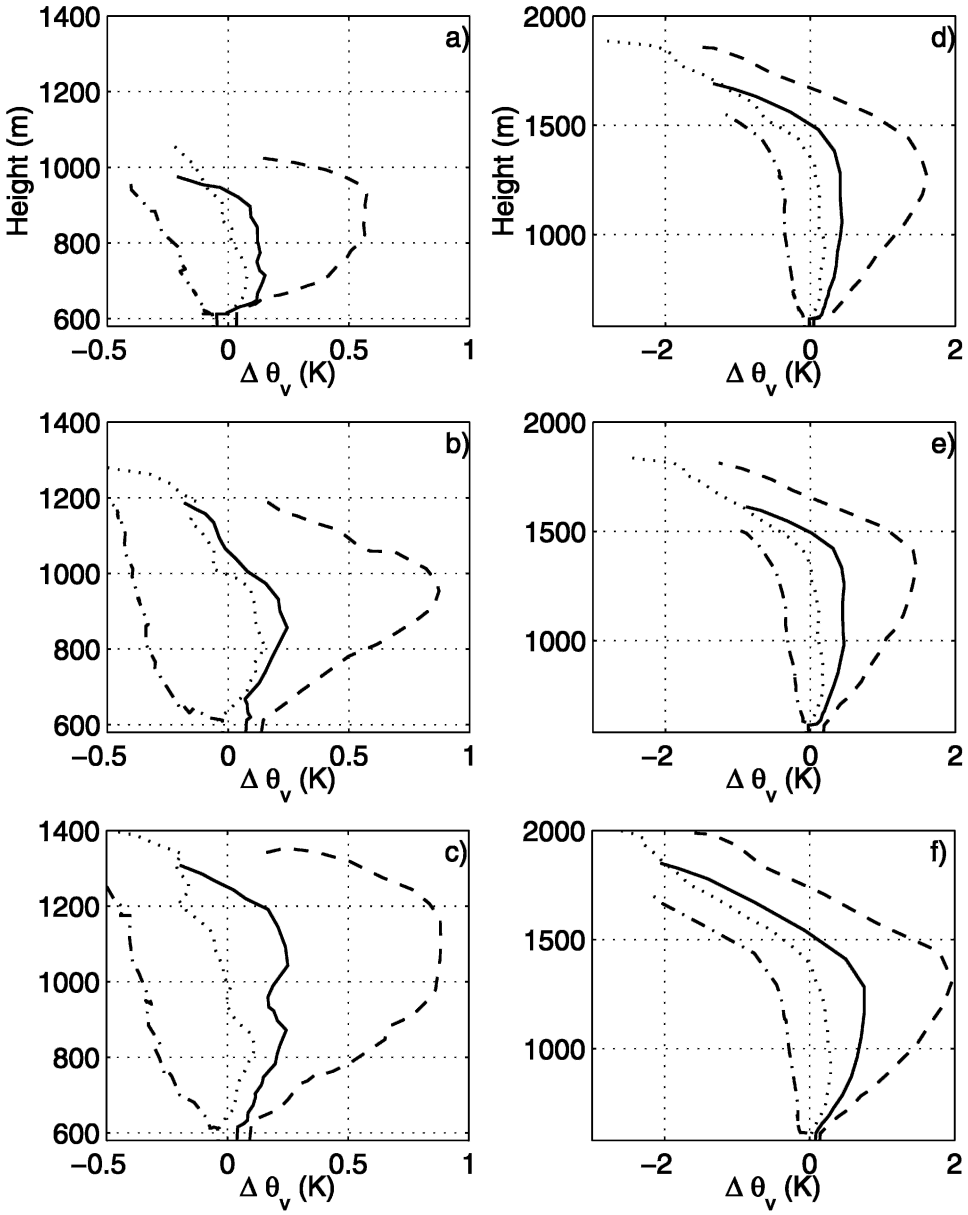

FIG. 11. (a)–(f) Vertical profiles/time histories of the buoyancy of the ACT mean (solid line), ACT core (dashed line), and the most dilute air (dotted–dash line) within ACTs for clouds A–F, respectively. The vertical height is the height of the geometric center of each region at 30-s time intervals. Dotted line: the vertical profile of the liquid water cloud lifetime mean buoyancy for each cloud (note the different scales between left and right panels).

enough to allow some air within the ACT to reach or overshoot its NBL without dilution. In this case, the cloud-top height will be solely determined by the ACT core thermodynamic properties and the environmental sounding. Another important feature shown in Fig. 13 is that the ACT size tends to decrease with height for small clouds (A, B, C) but stays relatively constant below the inversion and decreases above the inversion for large clouds. In no case does the ACT show a significant increase of size with height. This indicates that the ACT must detrain cloud environment mixtures as well as entraining environmental air throughout its ascent.

The buoyancy profiles of Fig. 11 indicate the inhomogeneous nature of the ACT interior. Figure 14 further shows the distributions of θ_l and q_t in the ACT of cloud E at several different heights (or times). Consistent with Fig. 11, the ACT is not uniformly diluted during its ascent. This would lead to a narrow distribution with mode properties that continuously shift toward environmental values with increasing height. In-

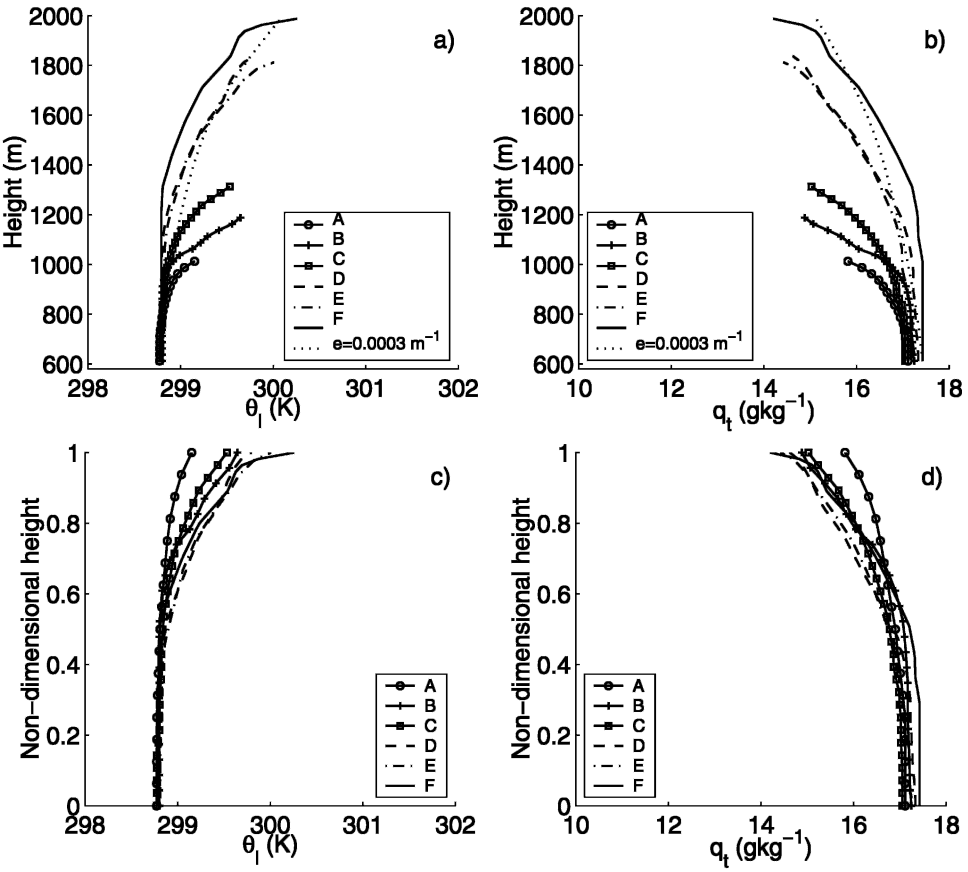

FIG. 12. Vertical profiles of θ_l and q_t for the ACT core for clouds A–F. (a) Liquid water potential temperature θ_l. Dotted line shows an entraining plume prediction with entrainment rate $e = 0.0003$ m^{-1} for comparison. (b) As in (a) but for the total water q_t. (c) As in (a) but normalized by the cloud-top heights for each cloud. (d) As in (c) but for q_t.

stead, the (θ_l, q_t) distributions maintain modes corresponding to a relatively undilute core with a tail continuously extending to environmental values, although the modes also show slight dilution above 1200 m. This mixture distribution and the mixing behavior of the ACT core in which there is little dilution until the ACT has traveled approximately two diameters, is consistent with the shedding thermal model of Blyth (1993) rather than a continuously entraining homogeneous plume model.

f. Passive mixing

The previous sections have focused on the kinematics and dynamics of individual ascending thermals, which may be viewed as fundamental elements or agents of cumulus convection. The ascending thermals are inherently nonsteady and produce the pulsating growth characteristic of the simulated clouds. The mixing behavior of ascending thermals controls the maximum cloud-top height and dominates the cloud upward vertical mass transport.

However, as noted above, during the ascent of an individual thermal a volume of more dilute cloudy air is left behind at the trailing wake. These mixtures may be generated either through the detrainment of ACT mixtures or simply by enhanced mixing in the wake of the ACT. They are characterized by small or negative buoyancy and low vertical velocity. To distinguish them from the active ascending element, we will refer to them as passive cloud mixtures. In contrast to the active ACT mixing, no distinctive coherent structures are observed in these passive cloud regions (compare, for example the velocity structure in Fig. 4 at 1100 m at 8.5 and 10.5 min). The continued mixing of this passive cloud results in more negative buoyancy and a net downward motion. As shown in Part I, much of the descent motion is realized in the unsaturated cloud mixed convective region in the simulated clouds.

Figure 15 shows an example of a cloud mixing life cycle at a fixed layer (1187.5–1312.5 m) that brackets the 1237.5-m vertical level shown in Fig. 1. Three joint distributions are plotted as functions of vertical velocity w and buoyancy $\Delta\theta_v$. Figure 15a shows contours of the joint frequency distribution (JFD) computed from the liquid-water-containing grid cells within the

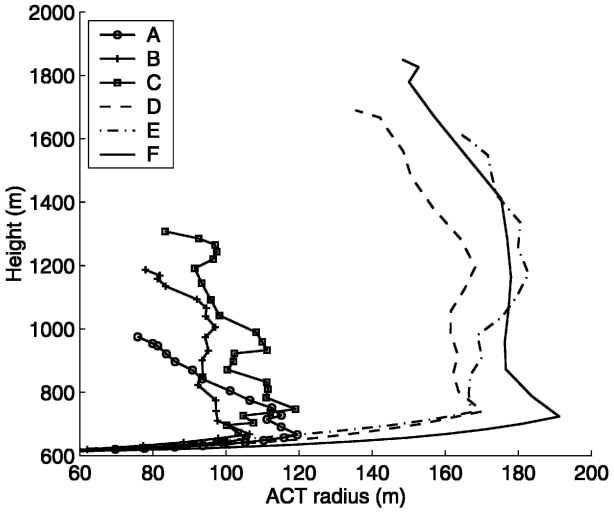

FIG. 13. Vertical profile of the spherical volume-equivalent radius of the ACT for clouds A–F.

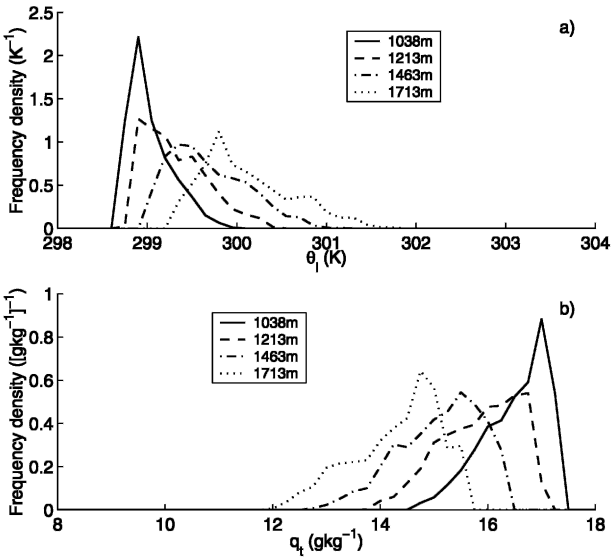

FIG. 14. Histograms of (a) θ_l and (b) q_t for all ACT grid cells for cloud E at four different heights (or equivalently, times). The legend heights show the ACT heights $z_T(t)$ at the selected times (390, 480, 570, and 660 s).

1187.5–1312.5-m layer during the life cycle of cloud E. Figures 15b,c show distributions of $\hat{q}_t$, the bin-averaged total water, and $\hat{t}$, the bin-averaged cloud mixture ages defined as the time since emergence of the cloud from the subcloud layer. The Fig. 15c contours show a steady increase in mixture age moving from the positively buoyant updrafts in the upper right of the figure to the negatively buoyant downdrafts in the lower left. Comparing this trend with Fig. 15b shows that the increase in mixture age is associated with a decrease in q_t, which indicates the dilution of cloud mixtures with time. Specifically, at about 600 s (upper right corner of Fig. 15c), the mixtures have $q_t \approx 16.2$ g kg^{-1} (Fig. 15b) with $\Delta\theta_v$ values greater than 1 K. Comparison of the three panels shows that the ACT arrives at this level as relatively undilute subcloud layer air with high values of total water ($\hat{q}_t > 16$ g kg^{-1}) and buoyancy ($\Delta\theta_v > 1$ K), with $\hat{q}_t$ dropping below 13.4 g kg^{-1} by the end of the cloud life cycle. Notice, however, the inhomogeneity of the ACT vertical velocity, which ranges between 1 and 6.5 m s^{-1} for bins along the 600-s contour. Examining (w, $\Delta\theta_v$) bins along a line of increasing $\hat{t}$ shows that, as time passes, there is a larger volume of more dilute cloudy air with low total water, buoyancy, and vertical velocity. Specifically, as $\hat{t}$ increases from 550 to 1200 s in Fig. 15c, the number of grid cells increases steadily (Fig. 15a), while the total water, buoyancy, and vertical velocity of those grid cells decreases (Fig. 15b). This progression is due to the continuous dilution of passive cloudy mixtures with environmental air; these mixtures become negatively buoyant and move downward as they age.

3. Discussion

We have simulated an ensemble of shallow cumulus clouds using an LES with an initial sounding and large-scale forcings consistent with the BOMEX field experiment. From this cloud ensemble we selected six individual clouds with cloud-top heights ranging from 1 to 2 km and, with the help of a subcloud tracer, observed their evolution from initial growth to final dissipation. In Part I we focused on the vertical mass flux profile in both the saturated and unsaturated convective mixed region. In this paper we have presented the kinematic and dynamic details of the saturated regions of the six clouds. All six clouds share these common features: 1) A growth phase that is characterized by the ascent of a single pulse (clouds A, B, C) or a series of pulses (clouds D, E, F) detached from the subcloud layer thermal. 2) A cloud-cap region that contains the largest values of horizontal divergence, vertical downward perturbation pressure gradient force (PPGF), and buoyancy. We refer to this as the ascending frontal cap (AFC); it is approximately 75 to 150 m thick in the simulated clouds. 3) A larger region extending through the cloud top that encompasses the coherent vortical internal (CT-relative) circulation. For the quantitative analyses we approximate this region by the upper ~175 m (small clouds) and ~350 m (large clouds). This ascending cloud top (ACT) is marked by a dynamic perturbation pressure pattern that is consistent with the vortical internal circulation. 4) A trailing wake characterized by passive cloud–environment mixtures with low values of vertical velocity and buoyancy. 5) A nearly constant thermal turnover time of approximately 600 s. 6) An ACT interior that has an inhomogeneous distribution of both thermodynamic properties and vertical momentum, with a relatively undilute core structure. 7) An ACT core that experiences no dilution dur-

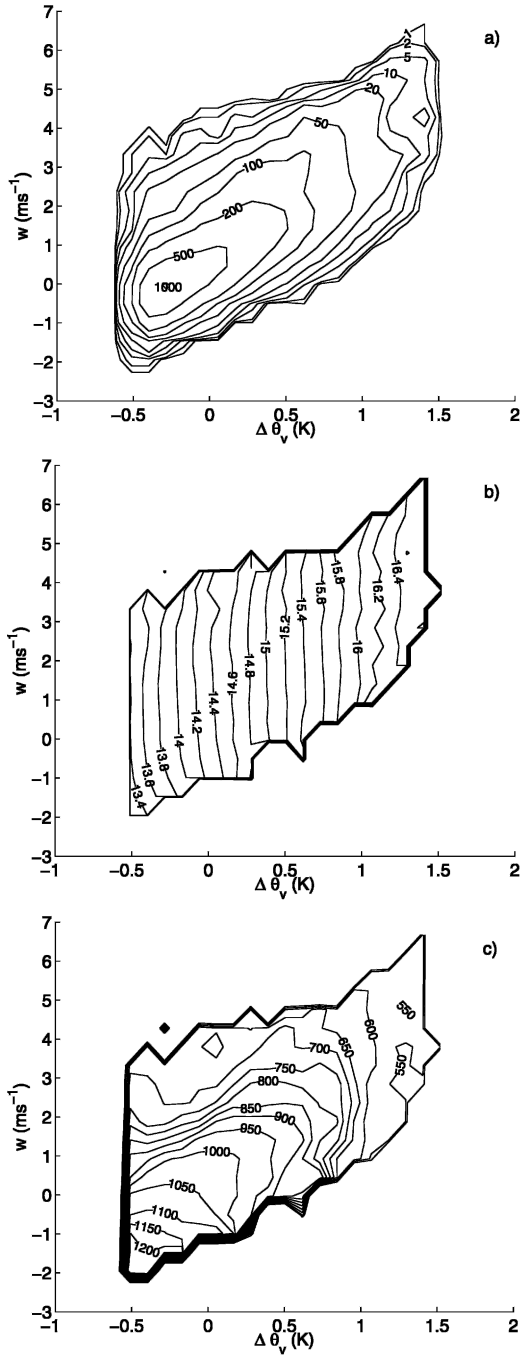

FIG. 15. An illustration of the mixing life cycle within a fixed cloud layer (between 1187.5 and 1312.5 m for cloud E). (a) Contours of the joint frequency distribution (unit: number of grid cells) of $\Delta\theta_v$ and w for the liquid water cloud region. (b) As in (a) but for the bin-averaged total water $\hat{q}_t$ (g kg^{-1}) for grid cells in each ($\Delta\theta_v$, w) bin. (c) As in (a) but for the bin-averaged cloud age $\hat{t}$ (unit: seconds) since emergence of the cloud from the subcloud layer.

ing the initial half of its ascent and gradual dilution during the later half of its ascent.

The elevated tracer experiment (Figs. 4–6) indicates that environmental air is entrained into the ACT both through its top and sides. Either route, however, is strongly modulated by the ACT's vortical circulation. The coherent ACT vortical circulation may be directly related to the horizontal buoyancy gradient within the ACT, which decreases from the ACT center to ACT edge, although the precise spatial distribution is far from symmetric (see Fig. 8). This horizontal buoyancy gradient produces a net torque, which tends to rotate the flow during its ascent. The result is an internal circulation where the ascent is along the central vertical axis while the descent is around its periphery. The vortical circulation drives the large-scale entraining eddies and wraps environmental air from the ACT rear into the rotating center where smaller-scale eddies produce further mixing. The large entraining eddies, which have scales comparable to the ACT size, dominate the ACT entrainment, mixing, and dilution. These eddies display a complex three-dimensional structure with a clear preference for enhanced entrainment and mixing at the downshear side of the clouds. For all simulated clouds, the ACT flow structure [calculated after removal of the cloud-top mean velocity ($w_T(t)$)] shows remarkable consistency with the dynamic perturbation pressure field (Fig. 9a). The strong downward PPGF within the AFC serves effectively as a lid for individual air parcels contained in the ACT and associates with the overturning motion, while the low pressure generated near the ACT edge serves as centripetal force for the vortical circulation (Yau 1979).

These simulation results, in combination with the cloud animations, paint the following picture of shallow cumulus mixing dynamics. The subcloud layer air tends to ascend in discrete elements that detach from their subcloud layer parent thermals. In contrast to the traditional parcel models (adiabatic or entraining plume), these ascending thermals both entrain and detrain on their way toward their maximum height. As a result of this continuous entrainment and detrainment, the ascending thermals are inhomogeneous both in their thermodynamic and dynamic properties. Note that, while the dilution of an individual ascending thermal may be continuous, the occurrence of each thermal in a cumulus cloud is typically episodic. For example, as shown in Fig. 1, the arrival of ascending thermals at a particular level is intermittent in both time and space. The dynamic perturbation pressure appears as the organizer of this group of inhomogeneous parcels. Specifically, it slows down fast-moving parcels and accelerates slow-moving parcels. The whole entity ascends at a speed approximately one-half that of the major updraft in the ACT center. The coherent vortical circulation strongly shapes the way that an ACT mixes with its environment. The coherence of the ACT mixing makes it qualitatively different from the dilution of passive cloud at the trailing wake of the ACT.

The vortical circulation of the simulated ACT is consistent with the laboratory results of ascending thermals across a range of stratifications (e.g., Scorer and Ronne

1956; Scorer 1957; Sanchez et al. 1989; Johari 1992). Our simulation shows, as do the recent laboratory results of Sanchez et al. and Johari, that the thermals that characterize shallow moist convection are not self-similar. Sanchez et al. (1989) found that the transition from an accelerating phase (near field) to a self-similar phase (far field) occurs when a thermal has traveled a distance of about six times its diameter. The maximum height reached by these simulated ACTs is typically four ACT diameters. This is possibly the reason that the hollow-cored thermals suggested by Scorer (1957) are not observed. Instead, the simulated ACT maintains a mushroomlike core with a shrinking stem containing the most undilute subcloud air.

These simulation results also strongly support the schematic shedding thermal model proposed by Blyth and coauthors (Blyth et al. 1988; Blyth 1993; Carpenter et al. 1998b). Blyth et al. (1988) proposed this ascending cloud-top mixing mechanism primarily to explain aircraft in situ observations showing that the conserved thermodynamic properties of cumulus mixtures tend to fall along a straight line between undilute subcloud air and environmental air near or above the observational level. Our numerical examination of the cloud kinematic structure, perturbation pressure field, and tracer transport provide more direct evidence of such mixing and its dominant role in the dynamics of these simulated clouds. The fact that none of the simulated ACTs undergo significant size increases during ascent indicates that the simulated ACTs must detrain as well as entrain. The distribution of ACT thermodynamic properties and the dilution history of the ACT core are also consistent with a mixing picture characterized by gradual core erosion and a continuous shedding of the ACT–environment mixtures during ascent, although the simulations also indicate that some mixed parcels may be carried upward for some distance before being shed in the ACT wake as either saturated or unsaturated mixtures.

The simulation results have indicated the important role of the dynamic perturbation pressure in the ACT's vertical momentum budget. A detailed understanding of ACT mixing is particularly relevant to questions about the ultimate height of an ascending thermal. We are currently using a Lagrangian analysis to examine the vertical momentum budget of the ACT and AFC. These results will be used to evaluate the impact of the vertical perturbation pressure gradient force and entrainment on the vertical momentum prediction, and therefore on the determination of cloud-top height.

Acknowledgments. We thank Marat Khairoutdinov for making his model available and for assistance with the case setup. The simulations were primarily performed using the facilities of the Geophysical Disaster Computational Fluid Dynamics Centre at the University of British Columbia; we thank Henryk Modzelewski for Beowulf cluster computing support. The manuscript was significantly improved by the comments of Steven Esbensen, Mark Holzer, Chin-Hoh Moeng, and two anonymous reviewers. This work was supported through funding of the Modeling of Clouds and Climate Proposal by the Canadian Foundation for Climate and Atmospheric Sciences, the Meteorological Service of Canada, and the Natural Sciences and Engineering Research Council. The first author gratefully acknowledges support from a University of British Columbia University Graduate Fellowship.

REFERENCES

Arakawa, A., and W. H. Schubert, 1974: Interaction of a cumulus cloud ensemble with the large-scale environment, Part I. *J. Atmos. Sci.,* **31,** 674–701.

Austin, P. H., M. B. Baker, A. M. Blyth, and J. B. Jensen, 1985: Small-scale variability in warm continental cumulus clouds. *J. Atmos. Sci.,* **42,** 1123–1138.

Barnes, G. M., J. Fankhauser, and W. D. Browning, 1996: Evolution of the vertical mass flux and diagnosed net lateral mixing in isolated convective clouds. *Mon. Wea. Rev.,* **124,** 2764–2784.

Blyth, A. M., 1993: Entrainment in cumulus clouds. *J. Appl. Meteor.,* **32,** 626–641.

——, and J. Latham, 1993: Development of ice and precipitation in New Mexican summertime cumulus clouds. *Quart. J. Roy. Meteor. Soc.,* **119,** 91–120.

——, W. A. Cooper, and J. B. Jensen, 1988: A study of the source of entrained air in Montana cumuli. *J. Atmos. Sci.,* **45,** 3944–3964.

Boatman, J., and A. H. Auer, 1983: The role of cloud-top entrainment in cumulus clouds. *J. Atmos. Sci.,* **40,** 1517–1534.

Bretherton, C. S., and P. K. Smolarkiewicz, 1989: Gravity waves, compensating subsidence, and detrainment around cumulus clouds. *J. Atmos. Sci.,* **46**, 740–759.

Carpenter, R. L., J. K. K. Droegemeier, and A. M. Blyth, 1998a: Entrainment and detrainment in numerically simulated cumulus congestus clouds. Part I: General results. *J. Atmos. Sci.,* **55,** 3417–3432.

——, ——, and ——, 1998b: Entrainment and detrainment in numerically simulated cumulus congestus clouds. Part III: Parcel analysis. *J. Atmos. Sci.,* **55,** 3440–3455.

Emanuel, K. A., 1981: A similarity theory for unsaturated downdrafts within clouds. *J. Atmos. Sci.,* **38,** 1541–1557.

——, 1991: A scheme for representing cumulus convection in large-scale models. *J. Atmos. Sci.,* **48,** 2313–2335.

——, 1994: *Atmospheric Convection.* Oxford University Press, 580 pp.

French, J. R., G. Vali, and R. D. Kelly, 1999: Evolution of small cumulus clouds in Florida: Observations of pulsating growth. *Atmos. Res.,* **52,** 143–165.

Grabowski, W. W., and T. L. Clark, 1993: Cloud–environment interface instability. Part II: Extension to three spatial dimensions. *J. Atmos. Sci.,* **50,** 555–573.

Heymsfield, A. J., P. N. Johnson, and J. E. Dye, 1978: Observations of moist adiabatic ascent in northeast Colorado cumulus congestus clouds. *J. Atmos. Sci.,* **35,** 1689–1703.

Holton, J. R., 1992: *An Introduction to Dynamic Meteorology.* Academic Press, 511 pp.

Jensen, J. B., P. H. Austin, M. B. Baker, and A. M. Blyth, 1985: Turbulent mixing, spectral evolution, and dynamics in a warm cumulus cloud. *J. Atmos. Sci.,* **42,** 173–192.

Johari, H., 1992: Mixing in thermals with and without buoyancy reversal. *J. Atmos. Sci.,* **49,** 1412–1426.

Jonas, P. R., 1990: Observations of cumulus cloud entrainment. *Atmos. Res.,* **25,** 105–127.

Khairoutdinov, M. F., and D. A. Randall, 2003: Cloud resolving

modeling of the ARM summer 1997 IOP: Model formulation, results, uncertainties, and sensitivities. *J. Atmos. Sci.,* **60,** 607–625.
Klaassen, G. P., and T. L. Clark, 1985: Dynamics of the cloud–environment interface and entrainment in small cumuli: Two-dimensional simulations in the absence of ambient shear. *J. Atmos. Sci.,* **42,** 2621–2642.
Ludlam, F. H., and R. S. Scorer, 1953: Convection in the atmosphere. *Quart. J. Roy. Meteor. Soc.,* **79,** 317–341.
Malkus, J. S., 1954: Some results of a trade-cumulus cloud investigation. *J. Meteor.,* **11,** 220–237.
——, and R. S. Scorer, 1955: The erosion of cumulus towers. *J. Meteor.,* **12,** 43–57.
Neggers, R., A. P. Siebesma, and H. Jonker, 2002: A multiparcel model for shallow cumulus convection. *J. Atmos. Sci.,* **59,** 1655–1668.
Paluch, I. R., 1979: The entrainment mechanism in Colorado cumuli. *J. Atmos. Sci.,* **36,** 2467–2478.
Raymond, D. J., and A. M. Blyth, 1986: A stochastic mixing model for nonprecipitating cumulus clouds. *J. Atmos. Sci.,* **43,** 2708–2718.
Sanchez, O., D. Raymond, L. Libersky, and A. Petschek, 1989: The development of thermals from rest. *J. Atmos. Sci.,* **46,** 2280–2292.
Saunders, P. M., 1961: An observational study of cumulus. *J. Atmos. Sci.,* **18,** 451–467.
Scorer, R. S., 1957: Experiments on convection of isolated masses of buoyant fluid. *J. Fluid Mech.,* **2,** 583–594.
——, 1958: *Natural Aerodynamics.* Pergamon Press, 313 pp.
——, and F. H. Ludlam, 1953: Bubble theory of penetrative convection. *Quart. J. Roy. Meteor. Soc.,* **79,** 94–103.
——, and C. Ronne, 1956: Experiments with convection bubbles. *Weather,* **11,** 151–155.
Siebesma, A. P., and J. Cuijpers, 1995: Evaluation of parametric assumptions for shallow cumulus convection. *J. Atmos. Sci.,* **52**, 650–666.
Squires, P., 1958: Penetrative downdraughts in cumuli. *Tellus,* **10,** 381–389.
Stith, J. L., 1992: Observations of cloud-top entrainment in cumuli. *J. Atmos. Sci.,* **49,** 1334–1347.
Stommel, H., 1947: Entrainment of air into a cumulus cloud. *J. Meteor.,* **4,** 91–94.
Taylor, G. R., and M. B. Baker, 1991: Entrainment and detrainment in cumulus clouds. *J. Atmos. Sci.,* **48,** 112–121.
Tiedtke, M., 1989: A comprehensive mass flux scheme for cumulus parameterization in large-scale models. *Mon. Wea. Rev.,* **117,** 1779–1800.
Warner, J., 1955: The water content of cumuliform cloud. *Tellus,* **7,** 449–457.
——, 1970: On steady-state one-dimensional models of cumulus convection. *J. Atmos. Sci.,* **27,** 1035–1040.
——, 1977: Time variation of updraft and water content in small cumulus clouds. *J. Atmos. Sci.,* **34,** 1306–1312.
——, and P. Squires, 1958: Liquid water content and the adiabatic model of cumulus development. *Tellus,* **10,** 390–394.
Wilhelmson, R., and Y. Ogura, 1972: The pressure perturbation and the numerical modeling of a cloud. *J. Atmos. Sci.,* **29,** 1295–1307.
Woodward, B., 1959: The motion in and around isolated thermals. *Quart. J. Roy. Meteor. Soc.,* **85,** 144–151.
Yau, M. K., 1979: Perturbation pressure and cumulus convection. *J. Atmos. Sci.,* **36,** 690–694.
Zhao, M., 2003: Episodic mixing and buoyancy-sorting representations of shallow cumulus convection. Ph.D. thesis, University of British Columbia, 219 pp.
——, and P. H. Austin, cited 2004: UBC cloud physics. [Available online at http://www.eos.ubc.ca/research/clouds.]
——, and ——, 2005: Life cycle of numerically simulated shallow cumulus clouds. Part I: Transport. *J. Atmos. Sci.,* **62,** 1269–1290.